

Coherent harmonic generation of magnons in spin textures

Received: 25 September 2023

Accepted: 22 January 2025

Published online: 30 January 2025

 Check for updates

Guibin Lan ^{1,2,9}, Kang-Yuan Liu^{1,2,9}, Zhenyu Wang ^{3,9}, Fan Xia^{1,2}, Hongjun Xu^{1,4}, Tengyu Guo⁴, Yu Zhang ^{1,2}, Bin He^{1,2}, Jiahui Li^{1,2}, Caihua Wan ^{1,2,4}, Gerrit E. W. Bauer ^{5,6}, Peng Yan ³ ✉, Gang-Qin Liu ^{1,4,7} ✉, Xin-Yu Pan^{1,4,7}, Xiufeng Han ^{1,4,8} & Guoqiang Yu ^{1,2,4} ✉

Harmonic generation, a notable non-linear phenomenon, has promising applications in information processing. For spin-waves in ferromagnetic materials, great progress has been made in the generation higher harmonics, however probing the coherence of these higher harmonics is challenging. Here, using in-situ diamond sensors, we study the coherent harmonic generation of spin waves in a soft ferromagnet. High-order resonance lines are generated via a microwave input and detected by nitrogen-vacancy (NV) centers in nanodiamonds. The phase coherence of the harmonic spin waves is verified by the Rabi oscillations of the NV electron spins. Numerical simulations indicate that the harmonic generation by microwaves below the ferromagnetic resonance frequency is associated with the nonlinear mixing of spin waves by magnetization structures at the film edge. Our finding of geometry-induced magnon harmonic generation constitutes a new way to generate magnon combs with coherent high-order harmonics and may pave the way for magnon-based information processing and quantum sensing applications.

Nonlinear phenomena are ubiquitous in nature, ranging from gravitational waves in the cosmos¹ to spin waves (or magnons) in nanomagnets^{2,3}. Among many intriguing nonlinear effects, harmonic generation is currently being intensively investigated. Because of appealing application prospects in information science and technology⁴, the higher harmonic generation of magnons has been pursued in a variety of magnetic systems^{5–12}. A recent breakthrough is the demonstration of the harmonic generation up to the sixtieth harmonic in a ferromagnetic film at very weak magnetic fields, which was ascribed to the spin-wave Cherenkov effect on top of the ripple pattern of the magnetization^{13,14}. However, the microscopic mechanism for the nonlinear spin-wave mixing is still elusive since the conceived spin-

wave Cherenkov effect has not been directly observed in experiment¹⁴. Nevertheless, previous theory has suggested that frequency multiplication can be realized in topological spin textures like domain walls¹⁵, skyrmions^{16–18}, and vortices¹⁹, because the large magnetization gradient can generate significant three-magnon processes that are indispensable for the formation of magnon frequency comb¹⁷. The extension of this mechanism to non-topological spin texture, like inhomogeneous edge magnetization, is still not clear.

The coherence of high-order spin waves generated by non-linear excitation is of vital importance if used as a source for coherent magnonic devices and information processing^{20,21}. For instance, one may use the phase of the spin wave for information exchange and

¹Beijing National Laboratory for Condensed Matter Physics, Institute of Physics, Chinese Academy of Sciences, Beijing, China. ²School of Physical Science, University of Chinese Academy of Sciences, Beijing, China. ³School of Physics and State Key Laboratory of Electronic Thin Films and Integrated Devices, University of Electronic Science and Technology of China, Chengdu, China. ⁴Songshan Lake Materials Laboratory, Dongguan, Guangdong, China. ⁵Kavli Institute for Theoretical Sciences, University of Chinese Academy of Sciences, Beijing, China. ⁶Advanced Institute for Materials Research (WPI-AIMR), Tohoku University, Sendai, Japan. ⁷CAS Center of Excellence in Topological Quantum Computation, Beijing, China. ⁸Center of Materials Science and Optoelectronics Engineering, University of Chinese Academy of Sciences, Beijing, China. ⁹These authors contributed equally: Guibin Lan, Kang-Yuan Liu, Zhenyu Wang.

✉ e-mail: yan@uestc.edu.cn; gqliu@iphy.ac.cn; guoqiangyu@iphy.ac.cn

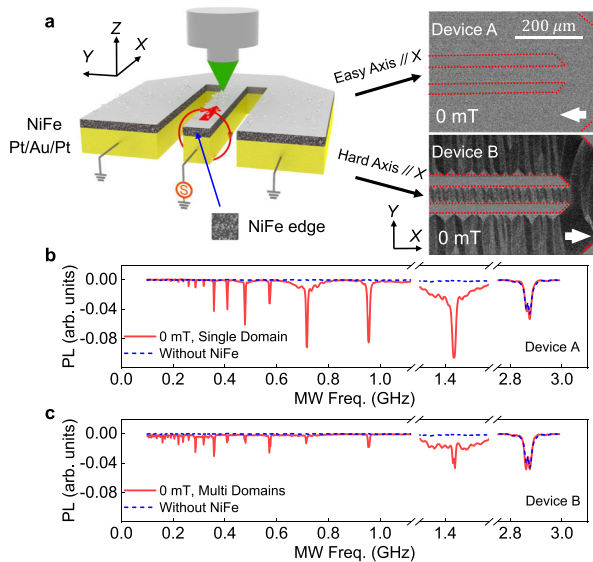


Fig. 1 | The measurement setup and measured ODMR spectra. **a** Left panel: device for the detection of harmonic generation with nanodiamonds, emphasizing the “edges” of the magnetic film. The red arrow indicates the magnetic field (when applied). The red circle ‘S’ represents the microwave input, which is connected to the signal line. The blue arrow indicates the location of the magnetic edge domains along the Y direction (smaller ones along the X direction do not contribute to the high-order spin wave generation). Right panel: Kerr microscopy images (scale bar, $200\ \mu\text{m}$) for signal line S (X axis) parallel to the easy axis (upper picture) and hard axis (lower picture), respectively, at $\mathbf{B}_{\text{ext}} = 0\ \text{mT}$ after reducing the external magnetic field along X from a large value ($\sim 26\ \text{mT}$) to zero (white arrows indicate magnetization directions in the underlying domain); **b**, **c** ODMR spectra for the two devices at $0\ \text{mT}$ and a non-magnetic reference. The driving rf power is $15.85\ \text{mW}$.

information processing without the Joule heating of charge transport²². For quantum information science, coherent spin waves provide an efficient route to realizing long-range quantum control of solid-state qubits (for example, color centers in diamond or SiC)^{23–29}. Propagating spin wave-based hybrid quantum sensors significantly extend the frequency detection range³⁰ and boost their sensitivity to magnetic signals^{31–36}. Despite these promising applications, it is a non-trivial task to probe the coherent nonlinear spin dynamics of a geometrically confined magnetic layer, as the stray field decays fast with the distance from the thin film, and in-situ magnetic probes with good spatial and temporal resolution are demanded.

Here, we report on the harmonic generation in a ferromagnetic film detected by nitrogen-vacancy (NV) centers in nanodiamonds that serve as in-situ quantum sensors. We demonstrate the harmonic generation of magnons in ferromagnetic films in single or multiple magnetic domain states that can be controlled by an external magnetic field. The generated high-order spin waves drive the Rabi oscillations of the NV electron spin, which provides solid evidence of the high quality of their phase coherence. Analytical calculations and micromagnetic simulations show that nonlinear spin-wave excitations nucleate in magnetic textures at the device edges.

Results

Sample characterization and measurement setup

The device and measurement setup are shown in the left panel of Fig. 1a. A ferromagnetic film (permalloy (Py), $\text{Ni}_{80}\text{Fe}_{20}$) is deposited on top of the coplanar waveguide (CPW) made of a Pt(5)|Au(100)|Pt(5) (thicknesses in nanometers) film. A magnetic field applied during the deposition in a magnetron sputtering chamber imprints an easy axis on the Py film. The vibrating sample magnetometer (VSM) measurements in Fig. S4 (Please refer to the Supplementary Information at ... (link) for technical details.) confirm the directions of easy and hard

axes. Two types of devices were fabricated, in which the signal line (along the X axis) is parallel to the easy (device A) and hard axis (device B), respectively. Finally, we deposited NV-center containing nanoscale diamond crystals (average diameter of $100\ \text{nm}$). A microwave-frequency (rf) electrical current generates rf magnetic fields that drive the magnetization precession in the Py. At the resonance frequency (f_{ESR}) of the NV electron spin, the photoluminescence (PL) of the NV centers exhibits dips that enable optically detected magnetic resonance (ODMR)^{37,38}. All the measurements we present were carried out at room temperature ($25 \pm 4^\circ\text{C}$) and a humidity of 30–40%.

Harmonic generation in the magnetic films

Figure 1b and c shows the ODMR spectra without an applied magnetic field for the two devices. The magnetization was initially saturated along the X axis by a magnetic field of $\sim 26\ \text{mT}$ that was subsequently reduced to zero. Because of the in-plane magnetic anisotropy, device A (device B) with an easy (hard) axis along the X axis settles into a single (multiple) domain state, as shown by the magneto-optic Kerr microscopy (MOKE) image in the right panel of Fig. 1a (see also Fig. S5 (Please refer to the Supplementary Information at ... (link) for technical details.)). We observe a clear frequency comb in the ODMR signal of both devices. The resonance dips appear at excitation frequencies of $2.87/n\ \text{GHz}$ (n is an integer), as reported previously¹⁴. The comb lines emerge when the NV resonance frequency $f_{\text{ESR}} (= 2.87\ \text{GHz}$ under zero field) is a multiple of the microwave frequency. At the first resonance dips ($n = 1$), the microwave field matches the ESR frequency of the NV spins, while all resonance dips with a frequency below $2.87\ \text{GHz}$ have to be attributed to the ferromagnetic layer. A microwave with a frequency of $1.43\ \text{GHz}$, for example, causes a signal via the stray field of a second harmonic magnon. Further evidence is the absence of the resonance dips in a non-magnetic reference sample (dotted blue line in Fig. 1b, c). We observe similar spectra for a CoFeB layer (see Fig. S6 (Please refer to the Supplementary Information at ... (link) for technical details.)), which shows the robustness of the phenomenon of harmonic generation of magnons in other magnetic materials. Importantly, the harmonic generation appears for both the single domain (see the top MOKE image of the right panel in Fig. 1a) and multidomain (see the bottom MOKE image of the right panel in Fig. 1a) states. Device A displays a stronger signal than device B under a zero magnetic field, as depicted in Fig. 1b, c. Below, we attribute this difference to the magnetic domain walls in device B that impede the propagation of spin waves generated at the edges and do not efficiently generate high-order harmonic spin waves¹⁵, even though domain walls, as nonuniform magnetic structures, are also considered as a source of high-order spin waves. The magnetic ripple domain thought to be essential in previous work¹⁴ is therefore not a necessary ingredient for the higher harmonic generation.

Magnetic field and microwave power dependence of harmonic generation

Next, we assess the effect of an applied magnetic field (\mathbf{B}_{ext}). Figure 2a shows the ODMR signals of device A when \mathbf{B}_{ext} is along the X axis (those of device B are referred to Fig. S7 (Please refer to the Supplementary Information at ... (link) for technical details.)). All the magnetic fields are set by scanning a large $\sim 26\ \text{mT}$ (larger than saturation field) to the target value. The high-order harmonic gradually decreases and eventually disappears with increasing \mathbf{B}_{ext} . Moreover, the high-order harmonics of device A appear at a lower magnetic field than in device B, presumably because of the additional magnetic anisotropy, as argued below.

According to Fig. 2b, c, an increasing microwave power enhances the features of the frequency comb (see also Fig. S12 (Please refer to the Supplementary Information at ... (link) for technical details.)). The direct excitation of the ESR and therefore the ODMR signal of the first resonance dip increases with power. The low-order resonance dips

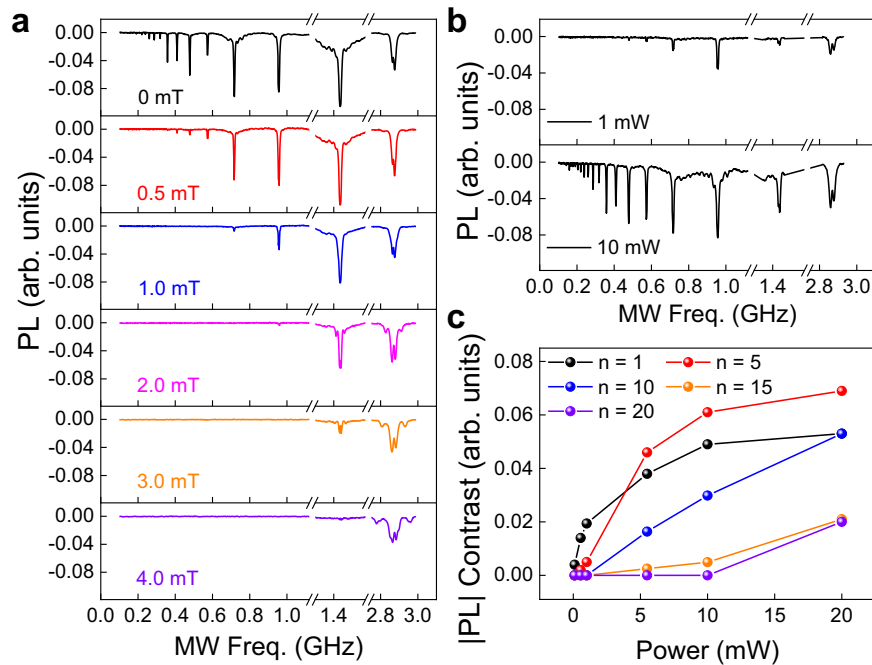


Fig. 2 | The magnetic field strength and power dependence of the frequency comb. **a** ODMR data for the device with signal line parallel to the easy X axis for $B_{\text{ext}} \in \{0 - 4.0\}$ mT. The driving rf power is 15.85 mW. **b** Power dependence

of ODMR spectra under zero magnetic field. The driving rf powers are 1 mW (upper panel) and 10 mW (lower panel). **c**, ODMR contrasts of higher-order signals with $n = 1, 5, 10, 15$ and 20 as a function of power.

show a similar power dependence, implying their excitation does not require a clear threshold, in contrast to, e.g., their parametric excitation. At even higher powers, the low-order harmonics saturate while higher-order resonance dips emerge gradually, consistent with the threshold-less harmonic generation predicted by micromagnetic simulations of topological magnetic textures¹⁷. The observed frequency comb is therefore the result of a nonlinear confluence of highly excited low frequency magnons.

Micromagnetic Simulations

We interpret the experimental findings with the help of micromagnetic simulations of a two-dimensional Py film with an easy X axis using the Mumax3.0 code³⁹. Decreasing the bias magnetic field from saturation to zero generates the initial magnetization displayed in Fig. 3a, where we have considered roughness along all edges of the device. A microwave field along Y with frequency $f_0 = 2.87/3$ GHz then drives the magnetization dynamics. Figure 3b shows the fast Fourier transformation (FFT) spectrum of the magnetization dynamics at the orange point in the bulk of the film in Fig. 3a. It reveals a series of resonance lines at the frequencies nf_0 as observed in the experiments. The stray fields at the edges are smaller than in the bulk, thereby causing a triangular-like potential that confines spin wave modes, also referred to as spin-wave well state^{40–42}, with frequencies below the bulk magnon gap. Moreover, inhomogeneous spin textures near the edges can significantly enhance the nonlinear spin-wave mixing^{15,16}. Therefore, the edge region efficiently generates higher harmonics. The harmonic generation disappears when there is no magnetic texture at the film edge, as shown in Fig. S15 (Please refer to the Supplementary Information at ... (link) for technical details.). We hence conclude that the inhomogeneous dipolar fields at the edges allow the formation of non-uniform magnetic textures. In these edge states, the cancellation of torques stabilizes low-frequency in-gap edge-bound magnon modes that are essential for the observed harmonic generation of up to 55 orders (see Figs. S8 and S9 (Please refer to the Supplementary Information at ... (link) for technical details.)). We also compute the dependences on the driving field amplitude. Spin-wave amplitude in

Fig. S17 (Please refer to the Supplementary Information at ... (link) for technical details.) increases with input power but saturates at a certain point. A larger ac field is required to reach saturation for high-order harmonics (0.5 mT for $n = 1$, 1.5 mT for $n = 2$, and 2.5 mT for $n = 3$), in agreement with the experimental results shown in Fig. 2c. As the harmonic generation effect is due to the nonlinear spin dynamics in a geometrically confined soft magnetic layer, it can be affected by the device geometry and damping constant of the permalloy. More details can be found in the Supplementary Materials (Please refer to the Supplementary Information at ... (link) for technical details.).

The second resonance peak in Fig. 3b is much weaker than the others. To understand this behavior, we plot the spin-wave dispersion along the X axis parallel to the external field $H_0 \hat{X}$. Micromagnetic simulations agree with the analytical formula (see black curve Fig. 3c)^{43–45}:

$$\omega = \sqrt{(A^* k^2 + \omega_H + \omega_K)(A^* k^2 + \omega_H + \omega_K + \omega_m F_p)} \quad (1)$$

where $A^* = 2\gamma A/M_s$ in terms of gyromagnetic ratio γ , exchange constant A , and saturated magnetization M_s . We also used $\omega_H = \gamma H_0$, $\omega_K = 2\gamma K_u/M_s$ with anisotropy constant K_u for an easy axis along \hat{X} , $\omega_m = \gamma\mu_0 M_s$, the dipole-dipole matrix element $F_p = 1 + g_k \cos^2 \theta_k + g_k(1 - g_k)/(\omega_H + \omega_K + A^* k^2)$ with $g_k = 1 - [1 - \exp(-kd)]/(kd)$ ⁴⁶, and Py film thickness d . The spin wave state with frequency $2f_0$ is a localized edge state in the magnon band gap, as shown in Fig. 3d. On the other hand, third and higher-order waves lie above the band gap and may propagate to the detection point deep in the film. It is noted that the dispersion of Damon-Eshbach (DE) magnons (propagating along the Y axis)⁴⁷ is much steeper (see blue curve in Fig. 3c) and is thus irrelevant to our experimental finding.

The coherence of higher harmonic generation

Next, we assess the phase coherence of the multiplied spin waves by time-dependent measurements of the NV electron spin Rabi oscillations. As shown in Fig. 4a, a 3- μ s green laser pulse initializes the NV spin

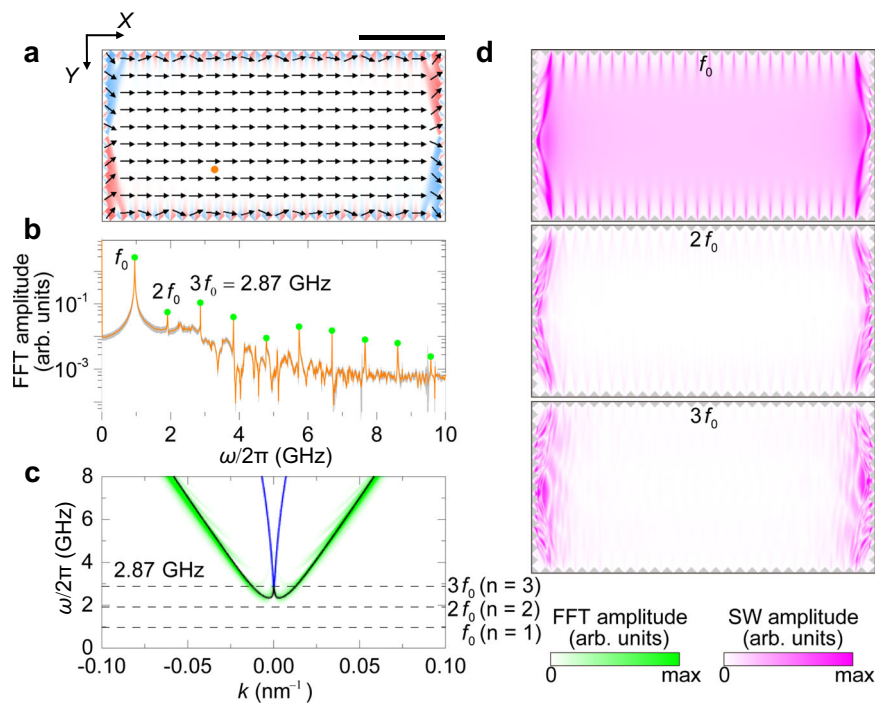


Fig. 3 | Micromagnetic simulations. **a** The static magnetization at 0 T after a magnetic field scan from a saturation field along the +X axis to zero. The orange dot is the detection position. (The scale bar in Fig. 3a is 5 μm) **(b)** The FFT spectrum of the computed magnetization time series at the orange dot marked in Fig. 3a under a microwave field with frequency $f_0 = 2.87/3$ GHz. The errors margins of the FFT spectrum are plotted as the gray region. **(c)** The dispersion relation of spin waves along the +X axis under a zero magnetic field. The green color and black curve are obtained from the simulations and Eq. (1), respectively. The blue curve depicts the dispersion of the surface spin waves⁴⁷. **(d)** The mode profiles of spin waves with the

frequencies f_0 , $2f_0$ and $3f_0$. f_0 is the frequency of an external RF magnetic field far below the spin wave gap of the bulk material (Fig. 3c) that resonates with the low-frequency edge modes. Since it penetrates the entire sample, it also reactively (non-dissipatively) drives the bulk magnetization as seen in the upper panel of Fig. 3d. The middle panel of Fig. 3d illustrates that the waves with frequency $2f_0$ below the band gap decay away from the edge. Those at $3f_0$ belong to the continuous spin-wave spectrum above the band gap and may propagate, as shown in the lower panel of Fig. 3d.

to the $m_s = 0$ states. Microwave pulses of different durations are then applied to manipulate NV spin state. A second laser reads out the final state through spin-dependent fluorescence. Figure 4c presents typical Rabi oscillations driven now by the second harmonic spin-wave ($f_{\text{ESR}}/2 = 1.417$ GHz) and different input powers. We also observed Rabi oscillation driven by the third harmonic spin wave (see Fig. 4d). The observed Rabi oscillations indicate that the high-order spin waves stay phase-coherent for at least a few hundred nanoseconds, which is an essential requirement for quantum control and related applications. The Rabi frequencies plotted as a function of the input microwave power (see Fig. 4e) illustrate the good efficiency of manipulating NV spin state by the higher-order AC stray fields as compared with Rabi oscillations of the same NV centers driven by the microwave directly ($f_{\text{ESR}} = 2.834$ GHz, Fig. 4a)³³. Both coherent and incoherent (thermal noise) spin waves coexist in the NiFe film, and the latter deteriorates the performance of possible quantum devices. Nevertheless, the demonstration of robust phase-coherence of the multiplied spin waves and the enlarged frequency detection window implies that a hybrid sensor composed of a NiFe film and NV centers could be useful for wide-band magnetic frequency of signal detection. The observation of coherent Rabi oscillations up to the third harmonic but absence at higher ones gives us an indication under what conditions higher harmonic modes lose their phase coherence. One physical reason is that, as the order increases, the magnon-magnon or magnon-phonon interactions act as an effective thermal bath for the high-order magnon, which causes significant dephasing effect. If the spin wave dephasing by magnon-magnon and magnon-phonon interactions or Joule heating through eddy currents prevents observation of the higher-order Rabi oscillations, we should repeat the experiments at low temperatures.

The proximity of the ferromagnet increases the attenuation of the coherent Rabi oscillations. The observed spin relaxation time $T_1 = 1.7 \pm 0.2 \mu\text{s}$ (Fig. 4f) of the NV centers on the NiFe film is about two orders of magnitude shorter than in bare nanodiamonds ($\sim 100 \mu\text{s}$)⁴⁸ because at the small bias magnetic fields (~ 6.4 mT), the magnetic noise of the NiFe film at the resonant frequency (2.768 GHz) stimulates the NV spin relaxation. The short T_1 time also explains why the Rabi oscillations driven by high-order spin waves occur only for a rather narrow window of the input power. The NV spin polarization should not decay on the scale of multiple coherent oscillations, which sets a lower bound for the input power, while the strong magnetic noise, on the other hand, suppresses the signals at high input powers. Numerical simulation indicates that strong driving fields bring large-angle deformation of the equilibrium magnetization (see Fig. S18 (Please refer to the Supplementary Information at ... (link) for technical details.)). Another possible reason is that higher intensities create additional magnetic textures (see simulation results in Fig. S19 (Please refer to the Supplementary Information at ... (link) for technical details.)). Another option would be harmonic spin wave generation by topologically protected spin textures such as skyrmions and hopfions, with possible higher coherence of the emitted spin waves.

Discussion

In summary, we report magnonic harmonic generation in a soft ferromagnet as detected by diamond NV center spectroscopy. The observed Rabi oscillation is evidence of good phase coherence of higher-order spin waves in our devices. Since the driving frequency is well below the magnon band gap, the nonlinear spin-wave mixing induced by the nonuniform magnetic structures at the film edge is instrumental. We thus exclude the domain-switching as the

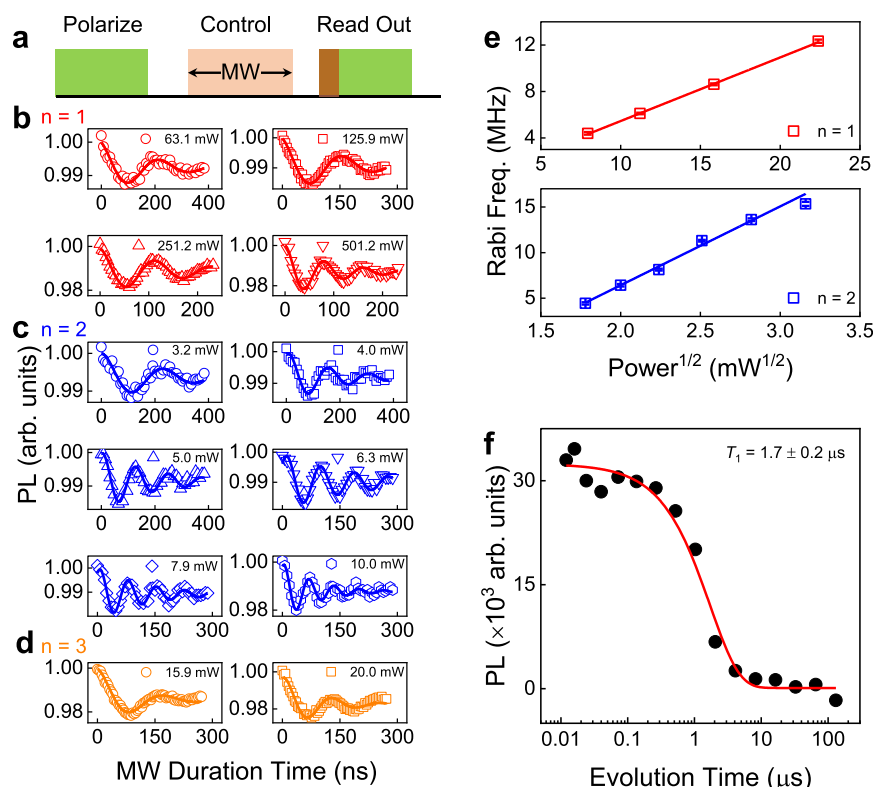


Fig. 4 | Phase coherence of higher spin-wave harmonics. **a** Pulse sequences to measure Rabi oscillation frequencies and spin relaxation times (T_1) of NV centers in diamonds. **b** Rabi oscillations driven by the 1st harmonic signal at different input powers. The applied microwave frequency is 2.834 GHz. **c** Rabi oscillations driven by the 2nd harmonic signal at different input powers. The applied microwave

frequency is 1.417 GHz. **d** Rabi oscillations driven by the 3rd harmonic signal at different input powers. The applied microwave frequency is 0.938 GHz. **e** Power dependence of the Rabi frequency, $n = 1$ is the 1st, and $n = 2$ is the 2nd harmonic. **f** Spin relaxation signal of the NV centers in the nanodiamond in Fig. 4a–f.

dominating origin for explaining the observed high-harmonic spin-waves. The spin-texture-induced magnon frequency comb may help open the door for magnon-based information processing and be beneficial to wide-band magnetic signal detection.

Methods

Films growth and sample preparation

The multilayer films were deposited on Si/SiO₂ wafers using magnetic sputtering systems with a base pressure of less than 8×10^{-7} Pa. To produce a uniform film, the sample must rotate at a rate of approximately $\pi/5$ rad/s during sputtering due to the tilted magnetron target. A permanent magnet attached to the sample holder induces a magnetic field of 0.18 mT, aligning the easy-axis or hard-axis of the magnetic films (NiFe and CoFeB) in a predetermined direction. The specific description of the devices and the relevant discussion about the two systems are shown in Table S2. The specific film growth conditions are shown in Table S1. The coplanar waveguides (CPWs) were patterned using ultraviolet (UV) lithography and the excess materials were subsequently removed through Ar ion milling. The detailed progress is depicted in Fig. S1. Figure S2 illustrates the structure of a device captured under optical microscopy.

Deposition of nanodiamonds

The nanodiamonds, which contain an ensemble of nitrogen-vacancy (NV) centers (Adámas Nanotechnologies, diameter ~100 nm, NV concentration ~3 ppm), are suspended in an isopropanol solution (5 $\mu\text{g}/\text{ml}$). The deposition of nanodiamonds was accomplished by transferring a drop of ~10 μl ND ethanol solution to the device with pipette. Nanodiamonds were deposited on the device surface after the volatilization of isopropanol.

NV magnetometry and Rabi oscillations

The nanodiamonds contain an ensemble of nitrogen-vacancy (NV) centers (Adámas Nanotechnologies, diameter ~100 nm, NV concentration ~3 ppm) and are deposited on the device described above. Measurements are performed in a home-built scanning confocal microscope setup, and the diagram of the ODMR system is shown in Fig. S3. Samples are illuminated by a green solid-state 532-nm laser (CNI, MLL-III-532-150mW) with a dedicated acousto-optic modulator (Gooch & Housego, 3350-199). The light is sent into a microscope frame (Olympus, IX73) equipped with dichroic mirrors and high-NA objectives (Olympus, MPlanFL N100X/0.9). The fluorescence signal is detected through a 650-nm long-pass filter (semrock) by an avalanche photodiode (Excelitas, APCM-700-10-FC). Scanning and positioning are realized by a 3-axis piezo-scanning stage (Physik Instrumente, E-727.3CDA). During the ODMR measurements, the signal generator (Rohde & Schwarz SMIQ06B, or Keysight N5183B) continuously sends microwaves (MW) into the device directly. The fluorescence counts of the NV centers are recorded as a function of the MW frequency. For the Rabi measurements, the MW signal is pulsed by an RF switch. A high-power MW amplifier (Mini-Circuits, ZHL-16W-43-s +) is used in measuring Rabi oscillations driven by resonant microwave pulses. The amplifier is not used when measuring the Rabi oscillations driven by high-order spin waves.

Measurement protocols and data analysis steps

Each measurement was started by initially saturating the magnetization along the X axis using a magnetic field of ~26 mT, and subsequently reducing it to zero. The ODMR spectra were measured by recording the photoluminescence (PL) counts of NV centers while the applied microwave frequency was swept. The integration time of each

microwave frequency is 1 ms, followed by a referenced count of the same duration (no MW). The measurement sequence was repeated 3000 times, and for each microwave frequency, the sum of signal counts was normalized by the sum of the referenced counts. To do so, we can eliminate quasi-static fluctuation of the laser power.

Model or data processing code

We carried the micromagnetic simulations out using the software package Mumax3.0 with RF field polarized along the y-direction. We discretized the film into cuboids of dimensions $10 \times 10 \times 20 \text{ nm}^3$. We consider a ferromagnetic film with dimensions $20 \times 10 \times 0.02 \mu\text{m}^3$, which is saturated by a bias magnetic field. Then, by decreasing the bias field from the saturation to zero, an initial state is obtained, as shown in Fig. 3a. A microwave field along y direction with frequency $f_0 = 2.87/3 \text{ GHz}$ is applied on the whole ferromagnetic film to drive the magnetization dynamics. By the fast Fourier transformation (FFT) of the dynamic magnetization component $\delta m_z(t)$ at the orange point in the bulk of the film in Fig. 3a, the spin-wave spectrum $\delta m_z(f)$ is obtained, as shown in Fig. 3b. The space distribution of spin-wave modes at resonance lines in Fig. 3d is extracted from the FFT spectrum of the dynamic magnetization over the whole film. The spin-wave dispersion in Fig. 3c is obtained by the FFT of the dynamic magnetization excited by a sinc-function field. Micromagnetic simulations are performed by using the software Mumax3.0. In Mumax3.0, the RF field along the y-direction can be easily applied via the code ' $B_{\text{ext}} = \text{vector}(0, h_0 \sin(2\pi f_0 t), 0)$ '. In simulations, a cuboid with the size $10 \times 10 \times 20 \text{ nm}^3$ was used to discretize the film sample. The present simulations do not account for defects, magnon-phonon coupling, or Joule heating that require further investigation.

Micromagnetic model parameters

Magnetic parameters used in micromagnetic simulations are as follows: the saturated magnetization $M_s = 8.6 \times 10^5 \text{ A/m}$, exchange constant $A = 13 \text{ pJ/m}$, uniaxial anisotropy constant $K_u = 2.53 \times 10^3 \text{ J/m}^3$ with the easy axis along the X direction, and the damping parameter $\alpha = 0.01$.

Data availability

All relevant data are available from the corresponding authors on request.

References

- Galtier, S. & Nazarenko, S. V. Direct evidence of a dual cascade in gravitational wave turbulence. *Phys. Rev. Lett.* **127**, 131101 (2021).
- Landau, L. D. & Lifshitz, E. M. On the theory of the dispersion of magnetic permeability in ferromagnetic bodies. *Phys. Z. Sowjetunion* **8**, 153–169 (1935).
- Gilbert, T. L. A phenomenological theory of damping in ferromagnetic materials. *IEEE Trans. Magn.* **40**, 3443–3449 (2004).
- Chumak, A. V. et al. Advances in magnetics roadmap on spin-wave computing. *IEEE Trans. Magn.* **58**, 1–72 (2022).
- Schultheiss, H. et al. Direct current control of three magnon scattering processes in spin-valve nanocontacts. *Phys. Rev. Lett.* **103**, 157202 (2009).
- Hermesdoerfer, S. J. et al. A spin-wave frequency doubler by domain wall oscillation. *Appl. Phys. Lett.* **94**, 223510 (2009).
- Demidov, V. E. et al. Generation of the second harmonic by spin waves propagating in microscopic stripes. *Phys. Rev. B* **83**, 054408 (2011).
- Demidov, V. E. et al. Resonant frequency multiplication in microscopic magnetic dots. *Appl. Phys. Lett.* **99**, 012505 (2011).
- Sebastian, T. et al. Nonlinear emission of spin-wave caustics from an edge mode of a microstructured $\text{Co}_2\text{Mn}_{0.6}\text{Fe}_{0.4}\text{Si}$ waveguide. *Phys. Rev. Lett.* **110**, 067201 (2013).
- Rousseau, O., Yamada, M., Miura, K., Ogawa, S. & Otani, Y. Propagation of nonlinearly generated harmonic spin waves in microscopic stripes. *J. Appl. Phys.* **115**, 053914 (2014).
- Groß, F. et al. Imaging magnonic frequency multiplication in nanostructured antidot lattices. *Phys. Rev. B* **106**, 014426 (2022).
- Zhang, H. et al. Spin-torque oscillation in a magnetic insulator probed by a single-spin sensor. *Phys. Rev. B* **102**, 024404 (2020).
- Yan, M., Kákay, A., Andreas, C. & Hertel, R. Spin-Cherenkov effect and magnonic Mach cones. *Phys. Rev. B* **88**, 220412 (2013).
- Koerner, C. et al. Frequency multiplication by collective nanoscale spin-wave dynamics. *Science* **375**, 1165–1169 (2022).
- Zhang, B., Wang, Z., Cao, Y., Yan, P. & Wang, X. R. Eavesdropping on spin waves inside the domain-wall nanochannel via three-magnon processes. *Phys. Rev. B* **97**, 094421 (2018).
- Aristov, D. N. & Matveeva, P. G. Stability of a skyrmion and interaction of magnons. *Phys. Rev. B* **94**, 214425 (2016).
- Rodrigues, D. R. et al. Nonlinear dynamics of topological ferromagnetic textures for frequency multiplication. *Phys. Rev. Appl.* **16**, 014020 (2021).
- Wang, Z. et al. Magnonic frequency comb through nonlinear Magnon-Skyrmion scattering. *Phys. Rev. Lett.* **127**, 037202 (2021).
- Wang, Z., Yuan, H. Y., Cao, Y. & Yan, P. Twisted magnon frequency comb and penrose superradiance. *Phys. Rev. Lett.* **129**, 107203 (2022).
- Pirro, P., Vasyuchka, V. I., Serga, A. A. & Hillebrands, B. Advances in coherent magnonics. *Nat. Rev. Mater.* **6**, 1114–1135 (2021).
- Yuan, H. Y., Cao, Y., Kamra, A., Duine, R. A. & Yan, P. Quantum magnonics: When magnon spintronics meets quantum information science. *Phys. Rep.* **965**, 1–74 (2022).
- Singh, S. D. et al. Temperature dependence of the photoluminescence from InP/GaAs type-II ultrathin quantum wells. *J. Phys. D: Appl. Phys.* **43**, 455410 (2010).
- Andrich, P. et al. Long-range spin wave mediated control of defect qubits in nanodiamonds. *npj Quantum Inf* **3**, 28 (2017).
- Trifunovic, L., Pedrocchi, F. L. & Loss, D. Long-distance entanglement of spin qubits via ferromagnet. *Phys. Rev. X* **3**, 041023 (2013).
- Fukami, M., Candido, D. R., Awschalom, D. D. & Flatté, M. E. Opportunities for long-range magnon-mediated entanglement of spin qubits via on- and off-resonant coupling. *PRX Quantum* **2**, 040314 (2021).
- Kikuchi, D. et al. Long-distance excitation of nitrogen-vacancy centers in diamond via surface spin waves. *Appl. Phys. Express* **10**, 103004 (2017).
- Rustagi, A., Bertelli, I., van der Sar, T. & Upadhyaya, P. Sensing chiral magnetic noise via quantum impurity relaxometry. *Phys. Rev. B* **102**, 220403 (2020).
- Simon, B. G. et al. Filtering and imaging of frequency-degenerate spin waves using nanopositioning of a single-spin sensor. *Nano Lett* **22**, 9198–9204 (2022).
- Borst, M. et al. Observation and control of hybrid spin-wave–Meissner-current transport modes. *Science* **382**, 430–434 (2023).
- Carmiggelt, J. J. et al. Broadband microwave detection using electron spins in a hybrid diamond-magnet sensor chip. *Nat. Commun.* **14**, 490 (2023).
- Sheng, L. et al. Nonlocal detection of interlayer three-magnon coupling. *Phys. Rev. Lett.* **130**, 046701 (2023).
- Van der Sar, T., Casola, F., Walsworth, R. & Yacoby, A. Nanometre-scale probing of spin waves using single electron spins. *Nat. Commun.* **6**, 8426 (2015).
- Du, C. et al. Control and local measurement of the spin chemical potential in a magnetic insulator. *Science* **357**, 195–198 (2017).
- Solanki, A. B. et al. Electric field control of interaction between magnons and quantum spin defects. *Phys. Rev. Research* **4**, L012025 (2022).

35. Bertelli, I. et al. Magnetic resonance imaging of spin-wave transport and interference in a magnetic insulator. *Sci. Adv.* **6**, eabd3556 (2020).
36. Prananto, D. et al. Probing thermal magnon current mediated by coherent magnon via nitrogen-vacancy centers in diamond. *Phys. Rev. Appl.* **16**, 064058 (2021).
37. Balasubramanian, G. et al. Nanoscale imaging magnetometry with diamond spins under ambient conditions. *Nature* **455**, 648–651 (2008).
38. Schirhagl, R., Chang, K., Loretz, M. & Degen, C. L. Nitrogen-vacancy centers in diamond: nanoscale sensors for physics and biology. *Annu. Rev. Phys. Chem.* **65**, 83–105 (2014).
39. Vansteenkiste, A. et al. The design and verification of MuMax3. *AIP Adv* **4**, 107133 (2014).
40. Jorzick, J. et al. Spin wave wells in nonellipsoidal micrometer size magnetic elements. *Phys. Rev. Lett.* **88**, 047204 (2002).
41. Fripp, K. G. & Kruglyak, V. V. Spin-wave wells revisited: From wavelength conversion and Möbius modes to magnon valleytronics. *Phys. Rev. B* **103**, 184403 (2021).
42. McMichael, R. D. & Maranville, B. B. Edge saturation fields and dynamic edge modes in ideal and nonideal magnetic film edges. *Phys. Rev. B* **74**, 024424 (2006).
43. Brächer, T., Pirro, P. & Hillebrands, B. Parallel pumping for magnon spintronics: Amplification and manipulation of magnon spin currents on the micron-scale. *Phys. Rep.* **699**, 1–34 (2017).
44. Kalinikos, B. A. & Slavin, A. N. Theory of dipolar-exchange spin wave spectrum for ferromagnetic films with mixed exchange boundary conditions. *J. Phys. C: Solid State* **19**, 7013 (1986).
45. Krivosik, P. & Patton, C. E. Hamiltonian formulation of nonlinear spin-wave dynamics: Theory and applications. *Phys. Rev. B* **82**, 184428 (2010).
46. Harte, K. J. Theory of magnetization ripple in ferromagnetic films. *J. Appl. Phys.* **39**, 1503 (1968).
47. Damon, R. & Eshbach, J. Magnetostatic modes of a ferromagnet slab. *J. Phys. Chem. Solids* **19**, 308–320 (1961).
48. Liu, G.-Q., Feng, X., Wang, N., Li, Q. & Liu, R.-B. Coherent quantum control of nitrogen-vacancy center spins near 1000 kelvin. *Nat. Commun.* **10**, 1344 (2019).

Acknowledgements

This work was financially supported by the National Key R & D Program of China (Grant Nos. 2022YFA1403602, 2019YFA0308100), the Science Center of the National Science Foundation of China (Grant No. 52088101), the National Natural Science Foundation of China (Grants Nos. 52161160334, 12274437, 12374103, 12434003, 12204089, 12074057, 12074422, 12374468, 12022509), the Innovation Program for Quantum Science and Technology (Grant No. 2023ZD0300600), the Strategic Priority Research Program of the Chinese Academy of Sciences (Grant Nos. XDB28000000, XDB33000000), the CAS Project for Young Scientists in Basic Research No. YSBR-084, the CAS Youth Interdisciplinary Team, and the JSPS KAKENHI Grants 19H00645, 22H04965.

Author contributions

G. L., K.-Y. L., Z. W., P. Y., G.-Q. L., and G. Y. conceived the idea for the experiment. G. L. performed the sample fabrication. K.-Y. L. and F. X. made the measurement by NV centers. Z. W. made the micromagnetic simulations. G. L., H. X., T. G., Y. Z., B. H., and J. L. made the electrical and magnetic measurements for the samples. G. L., K.-Y. L., and Z. W. performed the analysis with the help from C. W., G. E. W. B., P. Y., G.-Q. L., X.-Y. P., X. H., and G. Y.. G. L., K.-Y. L., Z. W., P. Y., G.-Q. L., and G. Y. wrote the manuscript and all the authors contributed to the final version.

Competing interests

The authors declare no competing interests.

Additional information

Supplementary information The online version contains supplementary material available at <https://doi.org/10.1038/s41467-025-56558-7>.

Correspondence and requests for materials should be addressed to Peng Yan, Gang-Qin Liu or Guoqiang Yu.

Peer review information *Nature Communications* thanks the anonymous reviewer(s) for their contribution to the peer review of this work. A peer review file is available.

Reprints and permissions information is available at <http://www.nature.com/reprints>

Publisher's note Springer Nature remains neutral with regard to jurisdictional claims in published maps and institutional affiliations.

Open Access This article is licensed under a Creative Commons Attribution-NonCommercial-NoDerivatives 4.0 International License, which permits any non-commercial use, sharing, distribution and reproduction in any medium or format, as long as you give appropriate credit to the original author(s) and the source, provide a link to the Creative Commons licence, and indicate if you modified the licensed material. You do not have permission under this licence to share adapted material derived from this article or parts of it. The images or other third party material in this article are included in the article's Creative Commons licence, unless indicated otherwise in a credit line to the material. If material is not included in the article's Creative Commons licence and your intended use is not permitted by statutory regulation or exceeds the permitted use, you will need to obtain permission directly from the copyright holder. To view a copy of this licence, visit <http://creativecommons.org/licenses/by-nc-nd/4.0/>.

© The Author(s) 2025